1	Intense Equatorial Electrojet and Counter Electrojet caused by the 15 January 2022 Tonga
2	Volcanic Eruption: Space and Ground-based Observations
3	
4 5 6 7	Guan Le <sup>1</sup> , Guiping Liu <sup>1,2,3</sup> , Endawoke Yizengaw <sup>4</sup> , Christoph R. Englert <sup>5</sup>
8 9	1. ITM Physics Laboratory, Heliophysics Division, NASA Goddard Space Flight
10	Center, Greenbelt, MD
11	<sup>2.</sup> The Catholic University of America, 620 Michigan Ave., N. E., Washington, DC
12	3. Space Sciences Laboratory, University of California, Berkeley, CA
13	<sup>4.</sup> Space Science Application Laboratory, The Aerospace Corporation, 2310 E. El
14	Segundo Blvd., El Segundo, CA
15	<sup>5.</sup> Space Science Division, U.S. Naval Research Laboratory, Washington, DC
16 17	
18	Submitted to Geophysical Research Letters on 4/5/2022
19	Paper Number: 2022GL099002
20	
21	
22	Key Points (maximum 140 characters per line):
23	• Space and ground-based observations reveal dramatic equatorial electrojet variations
24	caused by the Tonga volcanic eruption
25	• Strong eastward turning of atmospheric zonal winds in the E-region is responsible for the
26	directional reversal of the equatorial electrojet
27	• The observed complex spatiotemporal variations can be explained by a large-scale
28	disturbance propagating eastward from the eruption site
20	

#### Abstract

We present space and ground-based multi-instrument observations demonstrating the impact of the 2022 Tonga volcanic eruption on dayside equatorial electrodynamics. A strong counter electrojet (CEJ) was observed by Swarm and ground-based magnetometers on 15 January after the Tonga eruption and during the recovery phase of a moderate geomagnetic storm. Swarm also observed an enhanced equatorial electrojet (EEJ) preceding the CEJ in the previous orbit. The observed EEJ and CEJ exhibited complex spatiotemporal variations. We combine them with the Ionospheric Connection Explorer (ICON) neutral wind measurements to disentangle the potential mechanisms. Our analysis indicates that the geomagnetic storm had minimal impact; instead, a large-scale atmospheric disturbance propagating eastward from the Tonga eruption site was the most likely driver for the observed intensification and directional reversal of the equatorial electrojet. The CEJ was associated with strong eastward zonal winds in the E-region ionosphere, as a direct response to the lower atmosphere forcing.

## **Key Words**

- 46 Tonga Volcanic Eruption, Equatorial Electrojet, Counter Electrojet, Equatorial Electrodynamics,
- 47 Equatorial Electric Field, Atmospheric Neutral Winds

# **Plain Language Summary**

The Earth's E-region ionosphere (~100-150 km altitude) consists of both ionized and neutral gasses, and the two components are coupled through ion-neutral collisions. The state of this region is closely influenced by neutral atmospheric activities from the bottom and Sun's variability from the top. On 15 January 2022, the Tonga volcano had a massive eruption and injected enormous mass and energy into the atmosphere causing disturbances in the E-region ionosphere or even higher. There was also a moderate geomagnetic storm that started one day before the eruption and ended days after. These conditions offer a unique opportunity to understand the different roles they play in controlling the ionosphere. Coordinated observations including the atmosphere, ionosphere and magnetosphere were made from both space and on the ground during this event. We analyzed the magnetic field and neutral wind data and found that a large-scale atmospheric disturbance generated by the volcano eruption was responsible for the observed directional reversal of the dayside equatorial electric field and electric current.

Approved for public release. OTR 2022-00609.

#### 1. Introduction

63

64

65

66

67

68

69

70

71

72

73

74

75

76

77

78

79

80

81

82

83

84

85

The equatorial electrojet (EEJ) is an intense band of ionospheric electric current flowing eastward along the dayside magnetic equator within a narrow latitudinal extent. The peak of the EEJ occurs near the noon of the E-region ionosphere (~ 110 km altitudes), where a local maxima of the plasma density and conductivity is produced by the balanced acts between the photoionization from solar radiation and chemical losses (e.g., Heelis and Maute, 2020). The EEJ is a result of distinctive E-region electrodynamic processes involving both atmospheric neutrals and collisional plasma in a geometry with a horizontally northward geomagnetic field at the magnetic equator. During solar and geomagnetically quiet times, an eastward zonal electric field is generated in the dayside E-region by collisional interactions between neutrals and plasma as atmospheric tidal winds move ionospheric plasma across the magnetic field lines (known as Eregion neutral wind dynamo) (Richmond, 1973; Heelis, 2004). The current density of the EEJ can be readily measured in the magnetic field data both on the ground (Anderson et al., 2004; Yizengaw et al., 2014) or by the low-Earth orbit spacecraft (Lühr et al., 2004; Alken et al., 2015). Observations show that the EEJ exhibits much variability with longitude as well as in multiple temporal scales, from rapid large changes to diurnal, day-to-day, and seasonal variations e.g., Lühr et al., 2004; Yizengaw and Groves, 2018). Sometimes the EEJ can even experience directional reversals, known as counter electrojets (CEJ) (e.g., Forbes, 1981). The main causes of the EEJ variations are attributed to perturbations in the eastward electric field, which can be driven either from the top through enhanced solar wind-magnetosphere-ionosphere coupling (e.g., Yizengaw et al., 2016), or from the bottom side by neutral wind perturbations arising from the lower atmosphere wave forcing (e.g., Yamazaki et al., 2014). Variations of the EEJ have

been used as an indirect measure of the electric field perturbation in the dayside equatorial Eregion as well as at the F-region.

The main driving mechanism for the EEJ variability is the modulation of the E-region wind dynamo, through which the ionosphere strongly couples with the lower atmosphere forcing. Simultaneous spacecraft observations show that during the normal eastward EEJ the zonal winds across E-region altitudes are mostly in the westward direction whereas the winds reverse to be eastward at ~110 km altitude during the westward CEJ (Yamazaki et al., 2014). Vertically propagating atmospheric tidal waves can achieve sufficient amplitudes in the E-region at order of tens of m/s (e.g., Hagan and Forbes, 2002). These tidal winds directly produce the longitudinal and daily variations of EEJ (e.g., Forbes, 1981; Lühr et al., 2021). Large amplitude planetary waves such as 3-day waves have also been observed in the thermospheric wind field, and they could modulate the wind dynamo and thereby drive the multi-day periodic variations in the F-region ionosphere (e.g., Forbes et al., 2018; Liu et al., 2021). In addition, smaller-scale waves, such as gravity waves triggered by geological hazards of earthquake and tsunami etc., could induce short-period fluctuations in the EEJ and the electric fields (e.g., Aveiro et al., 2009;

Hysell et al., 1997).

Prompt penetration electric field (PPEF) during geomagnetically active times is an additional source of electric field variations in the low-latitude E-region ionosphere (e.g., Fejer et al., 1979; Wolf et al., 2007). During geomagnetic storms, extreme changes of the EEJ, both enhancement and directional reversals (CEJ), have been observed nearly instantaneously following the IMF changes and rapid variations of the Region-1 field-aligned currents (FACs) that lead to undershielding and overshielding conditions, respectively (Kelley et al., 1979; Kikuchi et al., Approved for public release. OTR 2022-00609.

108	2000; Sastri, 2002; Simi et al., 2012; Yizengaw et al., 2016; Astafyeva et al., 2019). High-

latitude ionosphere can also couple with the middle- and low-latitudes through disturbance winds during geomagnetic storms, known as disturbance dynamo (Fejer et al., 1983). Unlike the PPEF, disturbance dynamo electric fields have delayed responses to the high latitude heating events (Richmond and Matsushita, 1975).

On 15 January 2022, Swarm spacecraft observed a much enhanced EEJ and then a strong CEJ in two consecutive dayside equator passes (~ 1.5 hr apart). On the same day, a ground-based magnetometer pair near the magnetic equator in Peru, Jicamarca and Tarapoto, observed an intense CEJ first but then only the normal EEJ. The observed EEJ and CEJ in space and on the ground exhibited complex spatiotemporal variations. The event occurred during a period when both the magnetospheric forcing from the top and atmospheric forcing from the bottom coexisted: a moderate geomagnetic storm and the Tonga volcanic eruption, respectively. In this paper, we present a detailed analysis of the observations from multiple sources, including the IMF and solar wind, ground-based and spacecraft magnetic fields, and atmospheric neutral winds to determine the role of these potential sources on perturbing the equatorial E-region electric field. The goal is to disentangle the mechanisms responsible for the observed intensification and directional reversal of the equatorial electrojet.

125

126

124

109

110

111

112

113

114

115

116

117

118

119

120

121

122

123

# 2. Dataset Description

Swarm is a three-spacecraft mission launched into a high-inclination (87.5°) low-Earth orbit
on 22 November 2013 (Friis-Christensen et al., 2006). Swarm-A/C fly side by side at the same
altitude (~430 km at the start of 2022) with a longitudinal separation of 1.4° and Swarm-B in a
slightly higher altitude orbit (~500 km). With an orbit period of ~90 min, the spacecraft crosses
the polar cap every ~45 mins and the EEJ region every ~1.5 hrs. Highly accurate magnetic field

data from Swarm's Vector Field Magnetometer (VFM) provide high cadence in situ

measurements of FACs in the auroral zone (Lühr et al., 2015; 2016). The magnetic field strength

from the Absolute Scalar Magnetometer (ASM) measurements have been used to obtain the

amplitude and direction of the EEJ (Alken et al., 2015; Lühr et al., 2021).

Approved for public release. OTR 2022-00609.

The EEJ signals are also obtained from a pair of ground magnetometer stations located near the magnetic equator on the same meridian, one at the magnetic equator (within 3.5°) and the other one just off the EEJ region (6° to 9° degree from the magnetic equator) (Anderson et al.,

2004; Yizengaw et al., 2014). The EEJ currents are determined from δ♦♦ H, the difference of the magnetic field H-components between the two magnetometers. A detailed description of how to extract the EEJ from ground magnetometer observations can be found in Anderson et al. (2004) and Yizengaw et al. (2014). The pair of the ground stations we used in this study are located at Jicamarca (JICA, 11.95°N/76.87°W GEO, MLat=0.6°) and Tarapoto (TARA, 6.59°N/76.36°W GEO, Mlat= 6°) in Peru.

The neutral wind measurements are provided by the Michelson Interferometer for Global High-Resolution Thermospheric Imaging (MIGHTI) (Englert et al., 2017) on the 27° low-inclination Ionospheric Connection Explorer (ICON) mission (Immel et al., 2018). Using Doppler shifts, atmospheric wind velocities are derived from the O(¹S) (557.7 nm, green line) and O(¹D) (630.0 nm, red line) airglow emissions at ~3 and 10 km altitude bins, respectively across the range from ~90 to 300 km. The MIGHTI winds have been validated with the ground-

151	based measurements showing a correlation of ~0.8 (Harding et al., 2021; Makela et al., 2021).
152	The MIGHTI winds cover low-to-mid latitudes from ~13°S to 42°N, and for each day the data
153	are available from ~15 orbits with two local times sampled at the same latitude per orbit.

### 3. Observations

155

156

157

158

159

160

161

162

163

164

165

166

167

168

169

170

171

On 14 January 2022, a moderate geomagnetic storm (minimum Dst ~ -91 nT) was triggered by the arrival of the coronal hole high-speed solar wind stream. Figure 1 shows the 5-min resolution OMNI data with IMF/solar wind conditions and SYM-H index for 13-16 January. The start times for the storm main and recovery phases are indicated by the two black arrows on the top, respectively. The storm's main phase was caused by a gradual southward turning of the IMF Bz component which lasted for  $\sim 7$  hours ( $\sim 16-23$  UT on 14 January). The recovery phase started when the IMF Bz suddenly turned strongly northward associated with a minor shock and then fluctuated between northward and southward directions. It took about 5 days for the magnetosphere to fully recover. On 15 January, coincident with the early stage of the storm's recovery phase, a powerful, quasi-continuous eruption of Hunga Tonga-Hunga Ha'apai Volcano occurred about 65 km north of Tonga's main island, starting at ~0402 UT for about 12 hours, which is indicated as the magenta bar on the top of Figure 1. Atmospheric waves produced by the eruption were observed globally in the first few hours and circled the Earth multiple times subsequently (Yuen et al., 2022; Zhang et al., 2022). These are the background conditions under which the 15 January EEJ and CEJ events were observed.

Figure 2 presents an overview of the observations. Figure 2a displays 5 days of the magnetic

Approved for public release. OTR 2022-00609.

field perturbations (13-17 January) from Swarm A. The red traces are the azimuthal component
of the perturbations over the polar cap from Swarm A's VFM. The magnetic field perturbations
in high latitudes are mainly caused by FACs, and the azimuthal component (δB_FAC, positive
for westward deflection) is expected to bear the largest FAC signatures (Le et al., 2016). The
black traces in Figure 2a are the perturbations of the field strength during the equatorial crossing
over the EEJ region (within 10° latitude from the dayside magnetic equator) from Swarm A's

ASM. The eastward EEJ would cause a magnetic field depression ( $\delta \diamondsuit \diamondsuit B < 0$ ) and the westward CEJ

a field enhancement ( $\delta \diamondsuit \Leftrightarrow B>0$ ).

178

179

180

181

182

183

184

185

186

187

188

189

190

191

192

193

194

On 14 January, the magnitude of  $\delta B$  FAC was enhanced to  $\sim 500$  nT after the storm onset at ~ 16 UT. But the EEJ did not change markedly compared with the previous EEJ passes, indicating the lack of the penetration electric field. This is most likely due to the rather gradual southward turning of the IMF, under which conditions the shielding of the convection electric field in middle and low latitudes was still effective. The intensity of the EEJ remained relatively stable until around ~ 14 UT on 15 January, when a much enhanced EEJ was observed by Swarm, denoted by 1 in Figure 2a and the blue arrow on top of Figure 1. A very strong CEJ was observed subsequently by Swarm in the next dayside equatorial pass at around 15.5 UT, denoted by 2 in Figure 2a and the red arrow on top of Figure 1. Figure 2c shows an expanded view of the Swarm observation for 1200-1725 UT on 15 January, containing the observations from both Swarm A and B. Similar to Swarm A, Swarm B also observed the much enhanced EEJ and then the strong CEJ, but its  $\delta \diamondsuit \diamondsuit$  B magnitudes were smaller because of its higher altitude. The geographic locations of Swarm A and B for the dayside equatorial passes are shown in Figure 2d as the line segments in black and gray, respectively. The CEJ region at ~ 15.5 UT was observed to the west of the EEJ region observed at ~ 14 UT although Swarm's local time remained to be

- the same, near the local noon.
- Figure 2b shows the ground-based observations near the magnetic equator for 13-17 January.
- The solid black traces are for  $\delta \diamondsuit \diamondsuit H$ , the differences between the H-components recorded at the
- 198 geomagnetic equator (JICA) and off the equator (TARA). The red traces are the estimated  $E \times B$
- drift in the F-region based on  $\delta \diamondsuit \diamondsuit H$  using the technique described in Anderson et al. (2004). Note
- that the data from JICA and TARA were not recorded on 16 January, and we used the data from

Huancayo (HUA, 12.05°S/75.33°W GEO, Mlat=-0.63°) and San Juan (SJG, 18.11°N/66.15°W 201 GEO, Mlat= $28.79^{\circ}$ ) to obtain  $\delta \bullet \bullet \bullet H$  (dotted line). Since the location of SJG is not ideal for EEJ 202 203 estimation, these  $\delta \diamondsuit \diamondsuit H$  data are used only for obtaining general information about EEJ behaviors. 204 but not for quantitative comparison with the other days. The start times for the Tonga eruption 205 and the storm main and recovery phases are indicated by the arrows in the 14 January panel. We 206 note that the ground stations did not measure significantly different EEJ strengths between 13 207 and 14 January. In addition, no significant changes, instantaneous or delayed, were observed at 208 the storm onset and recovery on 14 January. These observations indicate that the storm's impact 209 on the equatorial electric field was minimal in this case, consistent with the Swarm observations. 210 On 15 January, JICA immediately entered a CEJ period with the strong magnetic field 211 depression ( $\delta \diamondsuit \Leftrightarrow H < 0$ ) at ~12 UT (~ 7 local time), which is about the same time as it entered the 212 normal EEJ region in previous days. This means the CEJ was probably already present before 213 ~12 UT. After ~ 4 hr, JICA transitioned into an EEJ region ( $\delta \diamondsuit \diamondsuit H > 0$ ) at ~15.5 UT (~10.5 local 214 previous 215 two days, so it appeared to be a nominal EEJ. During the following two days (16 and 17 216 January), only normal EEJ was observed. In Figure 2d, the geographic location of JICA is 217 marked as a red triangle. The CEJ was also observed on the ground to the west of the Swarm

	4
('HT	locations.

We now focus on how neutral wind perturbations caused the electric field perturbations. Or
15 January, ICON spacecraft observed neutral winds for the same regions and times as Swarm
and JICA. Figure 2d marks the locations (blue dots) and timings of the daytime low-latitude
zonal winds (from green-line emission, <90° Solar Zenith Angle, < 25° latitude) measured by
MIGHTI Due to the low-inclination MIGHTI samples a relatively wide range of longitudes

during each orbit pass. The zonal winds observed along 7 orbits (each ~1.5 hr apart and during <10 minutes time interval) are presented in Figure 3. The brown curve passing through JICA (red triangle) is a part of the circle centered at the Tonga eruption site, showing locations of equal distance from the eruption site. At ~14 UT, the ICON observations were located across the brown curve, MIGHTI and JICA would thus concurrently detect the wind perturbations propagating from the eruption site. The observations for a few hours before and after 14 UT are also shown.

224

225

226

227

228

229

230

231

232

233

234

235

236

237

238

239

240

241

Figures 3a and 3b display the zonal wind sequences and averaged profiles, respectively, observed at the given times and locations. The wind components have been transformed into the local magnetic coordinates assuming zero vertical winds. At ~14 UT, eastward winds dominated across the E-region altitudes from ~95-120 km, and the largest winds reached ~200 m/s with the averaged peak values of ~150 m/s. Strong eastward winds are thus observed in the E-region in coincident with the strong CEJ at JICA. Following this, the winds were weaker (<100 m/s) and tended to gradually turn westward at ~15.5 and 17 UT. The winds were also almost all westward throughout the altitude region at ~7.5 UT. From ~9 to 11 UT, the winds remained westward at most altitudes with few values barely being eastward around 105 km. Near 12 UT, both eastward and westward winds occurred around 67.5°W longitudes, showing the winds changed from strongly eastward to westward especially below ~110 km. This indicates the transition from the Approved for public release. OTR 2022-00609.

242	CEJ to EEJ. Figure 3c presents the sequence of zonal wind observations at ~103 km altitude
243	versus longitude. Compared to the day before (in black), the dayside zonal winds on 15 January
244	(blue) exhibited a large variation having strong eastward winds over ~60° - 120° W longitude.
245	This is again consistent with the directional turning from the EEJ to CEJ.
246	

### 4. Discussion

247

248

249

250

251

252

253

254

255

256

257

258

259

260

261

262

263

The observations presented in the previous section showed complex spatiotemporal variations of the CEJ and EEJ, which can be explained by a large-scale disturbance propagating eastward from the Tonga eruption site. As illustrated in Figure 4a, the light green and blue areas represent the leading and trailing fronts of the disturbance, respectively. The leading front is associated with a westward neutral wind perturbation, which reinforces the background westward wind in the dayside and causes an increase in the eastward electric field. This front is expected to result in an enhanced EEJ region that has been observed by Swarm. On the west, a strong eastward wind perturbation by the trailing front is opposite to the background wind and thus reverses the eastward electric field causing the directional reversal of the EEJ (i.e., CEJ) and downward vertical drift inferred by JICA. This explanation is further illustrated in Figure 4b and the timelines of the observed features are summarized as follows.

• At ~12.5 UT (Figure 4b – top panel): The wind disturbance fronts had moved to cross the day-night terminator and reached the ICON measurement locations, but yet to reach Swarm so that a nominal EEJ was observed by Swarm (see Figure 2c). However, JICA just emerged from the nightside and entered directly into the trailing front to start detecting the CEJ, but completely missed the leading front for the enhanced EEJ (Figure

2b). Because the ICON measurements were near the center of the disturbance moving
from trailing to leading fronts, eastward and then westward zonal winds were observed
(Figure 3a). Given that JICA observed the CEJ at the time ~8 hrs after the volcanic
eruption and the great circle distance is ~10,000 km from JICA to Tonga, the speed of the
propagating disturbance was estimated to be at least ~350 m/s. Because the CEJ may

have arrived before JICA turned into sunlit conditions, the disturbance could be propagating faster.

- At ~14 UT (Figure 4b, 2<sup>nd</sup> panel from the top): The disturbance fronts continued its eastward propagation. Swarm's next equatorial crossing cut through the leading front so that a much enhanced EEJ was observed (see Figure 2c). Based on Swarm A's timing (~10 hr) and the great circle distance from the eruption site (~14,000 km), the speed of the leading front was estimated to be ~400 m/s. JICA remained within the trailing front and thus still observed the CEJ (Figure 2b). At this time, ICON measurements were within the trailing front (and at the same distance to Tonga as JICA) and strong eastward zonal winds were observed (Figure 3), which is consistent with the CEJ observation at JICA. This convincingly demonstrated that the CEJ was caused by the Tonga eruption associated wind perturbation that changed the dayside zonal wind to eastward in the Eregion.
- At ~15.5 UT (Figure 4b 3<sup>rd</sup> panel from the top): Swarm crossed the equatorial region inside the trailing front and was able to detect the strong CEJ (see Figure 2c). However, the front almost moved away from JICA as the JICA meridian was exiting from the CEJ region into the normal EEJ region (Figure 2b). Based on these timings, the CEJ observations by JICA lasted for ~ 3 hr and the scale size of the disturbance should be in

269

270

271

272

273

274

275

276

277

278

279

280

281

282

283

284

285

287	the order of ~5,000 km. On the other hand, the location of the ICON measurements was
288	far to the west of the disturbance, near the terminator, and weaker winds were observed.
289 •	At ~17 UT (Figure 4b – bottom panel): The disturbance had propagated further east.
290	Both Swarm and JICA were completely outside the disturbance region to the west and

observed regular EEJ current (see Figures 2b and 2c). ICON was even further away from the disturbance and also near the terminator and thus observed weaker winds.

293

294

295

296

297

298

299

300

301

302

303

304

305

306

307

292

291

The disturbance responsible for the observed EEJ and CEJ signatures is most likely related to atmospheric gravity wave activities that were produced by the Tonga volcanic eruption and detected globally within the first few hours of the eruption (Yuen et al., 2022). This volcanic eruption generated a broad spectrum of atmospheric waves, such as gravity waves, that propagated into the upper atmosphere and even affected the F-region ionosphere (Zhang et al., 2022; Themens et al., 2022). By combining space and ground-based observations, our analysis shows that this disturbance propagated eastward from the volcano eruption site with a propagation speed in the order of ~350-400 m/s. We also found that the disturbance has a spatial scale size of ~5,000 km in which the zonal wind perturbation reached up to ~200 m/s. These fall within the features of gravity waves that have been identified before for driving F-region ionospheric irregularities (e.g. Yizengaw and Groves, 2020), as well as those reported for the Tonga volcanic eruption (Yuen et al., 2022; Zhang et al., 2022; Themens et al., 2022). Such a large wind disturbance should be able to significantly modify the E-region dynamo and cause the dramatic variations on equatorial electric field and current as the observations we present

# 5. Summary and Conclusions

311	We present multi-instrument observations demonstrating the impact of the 15 January 2022
312	Tonga volcanic eruption on dayside equatorial electrodynamics using magnetic field and neutral
313	wind data from Swarm, ground-based magnetometers, and ICON. The Tonga eruption coincided

with the early recovery phase of the 14-17 January 2022 geomagnetic storm. A strong CEJ was observed by both the Swarm satellites and JICA ground-based magnetometers on 15 January after the Tonga eruption and during the storm recovery phase. The CEJ observed by Swarm was preceded by a much enhanced EEJ in the previous orbit about 1.5 hr earlier. But JICA observed a normal EEJ after leaving the CEJ region. The EEJ and CEJ, observed both in space and on the ground, exhibited complex spatiotemporal variations. We linked the magnetic field observations in coincidence with atmospheric neutral wind observations from ICON to disentangle the potential mechanisms. Our analysis indicates that the moderate geomagnetic storm had minimal (almost no) impact on the equatorial electric field for this case. Instead, large-scale atmospheric disturbances propagating outward/eastward from the Tonga eruption site were the most likely driver for the observed intensification and directional reversal of the equatorial electrojet. We propose that the reversal of the equatorial electrojet is attributed to the strong eastward turning of atmospheric zonal winds in the E-region. While the leading wave front appeared to enhance the westward zonal winds responsible for the observed EEJ intensification, the trailing wave front caused strong eastward zonal winds resulting in the strong CEJ in the E-region ionosphere.

329

330

331

328

314

315

316

317

318

319

320

321

322

323

324

325

326

327

### **Data Availability Statement**

The IMF and solar wind data, as well as geomagnetic indices are available at the OMNIWeb at Approved for public release. OTR 2022-00609.

332	NASA Goddard Space Flight Center (GSFC) Space Physics Data Facility (SPDF),
333	https://omniweb.gsfc.nasa.gov. Swarm data are freely accessible to all users through ESA's
334	Earth Online site at <a href="https://earth.esa.int/eogateway/missions/swarm/data">https://earth.esa.int/eogateway/missions/swarm/data</a> . The ICON data are
335	publicly available from both the mission website at <a href="https://icon.ssl.berkeley.edu/Data">https://icon.ssl.berkeley.edu/Data</a> and
336	NASA/GSFC SPDF's Coordinated Data Analysis Web (CDAWeb) at

337	https://cdaweb.gsfc.nasa.gov/pub/data. The ground magnetometer data from JICA and TARA,
338	operated by LISN network, are publicly available at <a href="http://doi.org/10.5281/zenodo.6412518">http://doi.org/10.5281/zenodo.6412518</a> .
339	The ground magnetometer data from HUA and SJG are publicly available at INTERMAGNET
340	website at <a href="https://intermagnet.github.io">https://intermagnet.github.io</a> .
341	
342	Acknowledgements
343	We thank R. Pfaff, H. Lühr and T. Immel for helpful discussions. G. Liu was partially supported
344	by NASA grants 80NSSC20K1323 and 80NSSC18K0649. E. Yizengaw's work has been
345	partially supported by Air Force Office of Scientific Research (AFOSR) (FA9550-20-1-0119)
346	and NSF (AGS-1848730) grants. ICON was supported by NASA's Explorers Program through
347	contracts NNG12FA45C and NNG12FA42I.
348	
349	
350	
351	
352	
353	
354	
355 356 357	

- Alken, P., S. Maus, A. Chulliat, P. Vigneron, O. Sirol, and G. Hulot (2015), Swarm equatorial
- electric field chain: First results, Geophys. Res. Lett., 42, 673–680.
- 361 https://doi.org/10.1002/2014GL062658
- Anderson, D., A. Anghel, J. Chau, and O. Veliz (2004), Daytime vertical E × B drift velocities
- inferred from ground-based magnetometer observations at low latitudes, SpaceWeather, 2,
- 364 S11001. https://doi.org/10.1029/2004SW000095
- Astafyeva, E., I. Zakharenkova, and P. Alken (2016), Prompt penetration electric fields and the
- extreme topside ionospheric response to the June 22-23, 2015 geomagnetic storm as seen by
- the Swarm constellation, Earth, Planets and Space, 68:152. https://doi.org/10.1186/s40623-
- 368 016-0526-x
- 369 Aveiro, H.C., C.M. Denardini, & Abdu, M.A. (2009). Climatology of gravity waves-induced
- electric fields in the equatorial E- region. *Journal of Geophysical Research*, 114, A11308.
- 371 http://doi.org/10.1029/2009JA014177
- Englert, C.R., Harlander, J.M., Brown, C.M., Marr, K.D., Miller, I.J., Stump, J.E., Hancock, J.,
- Peterson, J.Q., Kumler, J., Morrow, W.H., Mooney, T.A., Ellis, S., Mende, S.B., Harris,
- 374 S.E., Stevens, M.E., Makela, J.J., Harding, B.J., & Immel, T.J. (2017). Michelson

375	Interferometer for Global High-resolution Thermospheric Imaging (MIGHTI): instrument
376	design and calibration. Space Science Reviews, 212(1-2), 553-584.
377	https://doi.org/10.1007/s11214-017-0358-4
378	Fejer, B. G., C. A. Gonzales, D. T. Farley, M. C. Kelley, and R. F. Woodman (1979), Equatorial
379	electric fields during magnetically disturbed conditions: The effect of the interplanetary
380	magnetic field, J. Geophys. Res.,84, 5797–5802. http://doi.org/10.1029/JA084iA10p05797

381	Fejer, B. G., M. F. Larsen, and D. T. Farley (1983), Equatorial disturbance dynamo electric
382	fields, Geophys. Res. Lett., 10, 537-540. <a href="https://doi.org/10.1029/GL010i007p00537">https://doi.org/10.1029/GL010i007p00537</a>
383	Forbes, J.M. (1981). The equatorial electrojet. Review of Geophysics, 19(3), 469-504.
384	https://doi.org/10.1029/rg019i003p00469
385	Forbes, J.M., Maute, A., Zhang, X., & Hagan, M.E. (2018). Oscillation of the ionosphere at
386	planetary-wave periods. Journal of Geophysical Research, 123,
387	https://doi.org/10.1029/2018JA025720
388	Friis-Christensen, E., H. Lühr, and G. Hulot (2006), Swarm: A constellation to study the Earth's
389	magnetic field, Earth Planets Space, 58, 351–358. <u>https://doi.org/10.1186/BF03351933</u>
390	Hagan, M.E., and Forbes, J.M. (2002). Migrating and nonmigrating diurnal tides in the middle
391	and upper atmosphere excited by tropospheric latent heat release. Journal of Geophysical
392	Research, 107(D24), 4754. https://doi.org/10.1029/2001JD001236
393	Harding, B.J., Chau, J.L., He, M., Englert, C.R., Harlander, J.M., Marr, K.D., et al. (2021).
394	Validation of ICON-MIGHTI thermospheric wind observations: 2. Green-line comparisons
395	to specular meteor radars. Journal of Geophysical Research, 126, 2020JA028947.
396	https://doi.org/10.1029/2020JA028947
397	Heelis, R.A. (2004). Electrodynamics in the low and middle latitude ionosphere: a tutorial.

Approved for public release. OTR 2022-00609.

398	Journal of Atmospheric and Solar-Terrestrial Physics, 66, 825-838.
399	https://doi.org/10.1016/j.jastp.2004.01.034
400	Heelis, R. A., & Maute, A. (2020). Challenges to understanding the Earth's ionosphere and
401	thermosphere. Journal of Geophysical Research: Space Physics, 125, e2019JA027497.
402	https://doi.org/10.1029/2019JA027497

403	Hunsucker, R. D (1982), Atmospheric gravity waves generated in the high-latitude ionosphere:
404	A review, Reviews of Geophysics, 20, 293-315. <a href="https://doi.org/10.1029/RG020i002p00293">https://doi.org/10.1029/RG020i002p00293</a>
405	Hysell, D.L., J.L. Chau, & Fesen, C.G. (2002). Effects of large horizontal winds on the
406	equatorial electrojet. Journal of Geophysical Research, 107(A8), SIA 27-1-SIA 27-12.
407	https://doi.org/10.1029/2001JA000217
408	Hysell, D. L., M. F. Larsen, and R.F. Woodman (1997). JULIA radar studies of electric fields in
409	the equatorial electrojet, Geophys. Res. Lett., 24 (13) (1997), pp. 1687-1690.
410	https://doi.org/10.1029/97GL00373
411	Immel, T.J., England, S.L., Mende, S.B. et al. (2018). The Ionospheric Connection Explorer
412	mission: mission goals and design. Space Science Reviews, 214.
413	https://doi.org/10.1007/s11214-017-0049-2
414	Kelley, M. C., B. G. Fejer, and C. A. Gonzales (1979), An explanation for anomalous equatorial
415	ionospheric electric fields associated with a northward turning of the interplanetary magnetic
416	field, Geophys. Res. Lett., 6, 301. http://doi.org/10.1029/GL006i004p00301
417	Kikuchi, T., H. Luhr, T. Kitamura, O. Saka, and K. Schlegel (1996), Direct penetration of the
418	polar electric fields to the equator during a DP 2 event as detected by the auroral and
419	equatorial magnetometer chains and the EISCAT radar, J. Geophys. Res., 101, 17,161-

420 17,173. https://doi.org/10.1029/96JA0129
--

- 421 Kikuchi, T., H. Luhr, K. Schlegel, H. Tachihara, M. Shinohara, and T.L. Kitamura (2000),
- Penetration of auroral electric fields to the equator during a substorm, *J. Geophys. Res.*, 105,
- 423 23,251–23,252. https://doi.org/10.1029/2000JA900016

424	Le, G., et al. (2016), Magnetopause erosion during the 17 March 2015 magnetic storm: Combined
425	field-aligned currents, auroral oval, and magnetopause observations, Geophys. Res. Lett.,
426	43. https://doi.org/10.1002/2016GL068257
427	Liu, G., England, S. L., Lin, C. S., Pedatella, N. M., Klenzing, J. H., Englert, C. R., et al. (2021).
428	Evaluation of atmospheric 3-day waves as a source of day-to-day variation of the
429	ionospheric longitudinal structure. Geophysical Research Letters, 48, e2021GL094877.
430	https://doi.org/10.1029/2021GL094877
431	Lühr, H., J. Park, J. W. Gjerloev, J. Rauberg, I. Michaelis, J. M. G. Merayo, and P. Brauer
432	(2015), Field-aligned currents' scale analysis per-formed with the Swarm constel-
433	lation, Geophys. Res. Lett., 42, 1–8. <a href="http://doi.org/10.1002/2014GL062453">http://doi.org/10.1002/2014GL062453</a>
434	Lühr, H., T. Huang, S. Wing, G. Kervalishvili, J. Rauberg, and H. Korth (2016), Filamentary
435	field-aligned currents at the polar cap region during northward interplanetary magnetic field
436	derived with the Swarm constellation, Ann. Geophys., 34, 901–915.
437	https://doi.org/10.5194/angeo-34-901-2016
438	Lühr, H., Zhou, YL., & Alken, P. (2021). Short-term variability of equatorial electrojet
439	modulation by solar tidal and planetary waves, as derived from the Swarm constellation.
440	Journal of Geophysical Research: Space Physics, 126, e2020JA028884.

441	https://doi.org/10.1029/2020JA028884
442	Makela, J. J., Baughman, M., Navarro, L. A., Harding, B. J., Englert, C. R., Harlander, J. M., et
443	al. (2021). Validation of ICON-MIGHTI thermospheric wind observations: 1. Nighttime
444	Red-line Ground-Based Fabry-Perot Interferometers. Journal of Geophysical Research, 126
445	https://doi.org/10.1029/2020JA028726

446	Richmond, A. D. (1973), Equatorial electrojet-1. Development of a model including winds and
447	instabilities, J. Atmos. Terr. Phys., 35, 1083–1103. https://doi.org/10.1016/0021-
448	9169(73)90007-X
449	Richmond, A. D. (2021). Joule heating in the thermosphere. In W. Wang, & Y. Zhang (Eds.),
450	Eds., Space physics and aeronomy collection volume 4. Upper atmosphere dynamics and
451	energetics, Geophysical Monograph Series (Vol. 261). AGU.
452	https://doi.org/10.1002/9781119815631.ch1
453	Richmond, A. D., and S. Matsushita (1975), Thermospheric Response to a Magnetic Substorm,
454	J. Geophys. Res., 80, 2839-2850. <a href="https://doi.org/10.1029/JA080i019p02839">https://doi.org/10.1029/JA080i019p02839</a>
455	Sastri, J. H., R. Sridharan, and T. K. Pant (2003), Equatorial ionosphere thermosphere system
456	during geomagnetic storms, in Disturbances in Geospace: The Storm-Substorm
457	Relationship, Geophys. Monogr. Ser.,vol. 142, edited by A. S. Sharma, Y. Kamide, and G.
458	S. Lakhina, pp. 185–203, AGU, Washington, D. C <a href="https://doi.org/10.1029/142GM16">https://doi.org/10.1029/142GM16</a>
459	Simi, K. G., S. V. Thampi, D. Chakrabarty, B. M. Pathan, S. R. Prabhakaran Nayar, and T.
460	Kumar Pant (2012), Extreme changes in the equatorial electrojet under the influence of
461	interplanetary electric field and the associated modification in the low-latitude F region
462	plasma distribution, J. Geophys. Res.,117, A03331. https://doi.org/10.1029/2011JA017328

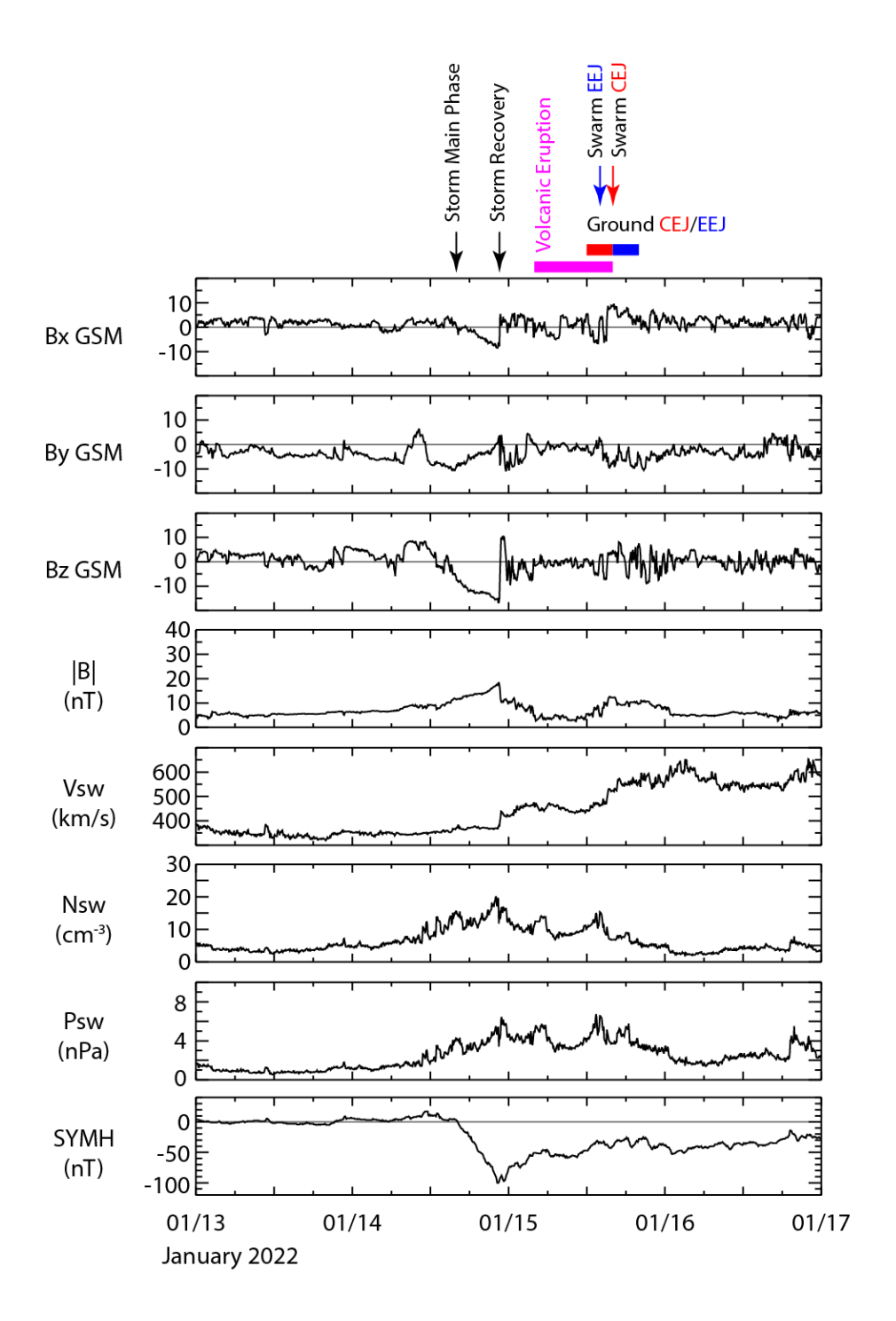
463	Somayajulu, V. V., C. A. Reddy, and K. S. Viswanathan (1987), Penetration of magnetospheric
464	convective electric field to the equatorial ionosphere during the substorm of March 22, 1979
465	Geophys. Res. Lett., 14, 876-879. <a href="https://doi.org/10.1029/GL014i008p00876">https://doi.org/10.1029/GL014i008p00876</a>
466	Themens, D.R., Watson, C., Zagar, N., Vasylkevych, S., Elvidge, S., McCaffrey, A., Prikryl P.,
467	Reid, B., Wood A., & Jayachandran P.T. (2022). Global propagation of ionospheric

468	disturbances associated with the 2022 Tonga volcanic eruption. Geophysical Research
469	Letters., https://doi.org/10.1029/2022GL098158
470	Wolf, R. A., R.W. Spiro, S. Sazykin, and F.R.Toffoletto (2007), How the Earth's inner
471	magnetosphere works: An evolving picture, Journal of Atmospheric and Solar-Terrestrial
472	Physics, 69, 288–302. <u>https://doi.org/10.1016/j.jastp.2006.07.026</u>
473	Yamazaki, Y., A. D. Richmond, A. Maute, HL. Liu, N. Pedatella, and F. Sassi (2014), On the
474	day-to-day variation of the equatorial electro-jet during quiet periods, J. Geophys. Res.
475	Space Physics,119, 6966–6980. <a href="http://doi.org/10.1002/2014JA020243">http://doi.org/10.1002/2014JA020243</a>
476	Yizengaw, E., & Groves, K. M. (2018), Longitudinal and seasonal variability of equatorial
477	ionospheric irregularities and electrodynamics, Space Weather, 16, 946-968.
478	https://doi.org/10.1029/2018SW001980
479	Yizengaw, E., M. B. Moldwin, E. Zesta, C. M. Biouele, B. Damtie, A. Mebrahtu, B. Rabiu, C. F.
480	Valladares, and R. Stoneback (2014), The longitudinal variability of equatorial electrojet
481	and vertical drift velocity in the African and American sector, Ann. Geophys., 32, 231–238.
482	https://doi.org/10.5194/angeo-32-231-2014
483	Yizengaw, E., M. B. Moldwin, E. Zesta, M. Magoun, R. Pradipta, C. M. Biouele, A. B. Rabiu,
484	O. K. Obrou, Z. Bamba, and E. R. de Paula (2016), Response of the equatorial ionosphere to

Approved for public release. OTR 2022-00609.

185	the geomagnetic DP 2 current system, Geophys. Res. Lett., 43, 7364–7372.
186	https://doi:10.1002/2016GL070090
187	Yuen, D.A., Scruggs, M.A., Spera, F.J., Zheng, Y., Hu, H., McNutt, S.R., Thompson, G.,
188	Mandli, K., Keller, B.R., Wei, S.S., Peng, Z., Zhou, Z., Mulargia, F., Tanioka, Y., Under the
189	Surface: Pressure-Induced Planetary-Scale Waves, Volcanic Lightning, and Gaseous Clouds
190	Caused by the Submarine Eruption of Hunga Tonga-Hunga Ha'anai Volcano Provide an

491	Excellent Research Opportunity, Earthquake Research Advances.
492	https://doi.org/10.1016/j.eqrea.2022.100134
493	Zhang, SR., Vierinen, J., Aa, E., Goncharenko, L.P., Erickson, P.J., Rideout, W., Coster, A.J.,
494	& Spicher, A. (2022). 2022 Tonga volcanic eruption induced global propagation of
495	ionospheric disturbances via Lamb waves. Frontiers in Astronomy and Space Sciences,
496	9:871275. https://doi.org/10.3389/fspas.2022.87125
497	



498 Figure 1

Figure 1. The 5-min resolution OMNI data with IMF/solar wind conditions and SYM-H index for 13-16 January 2022.

499

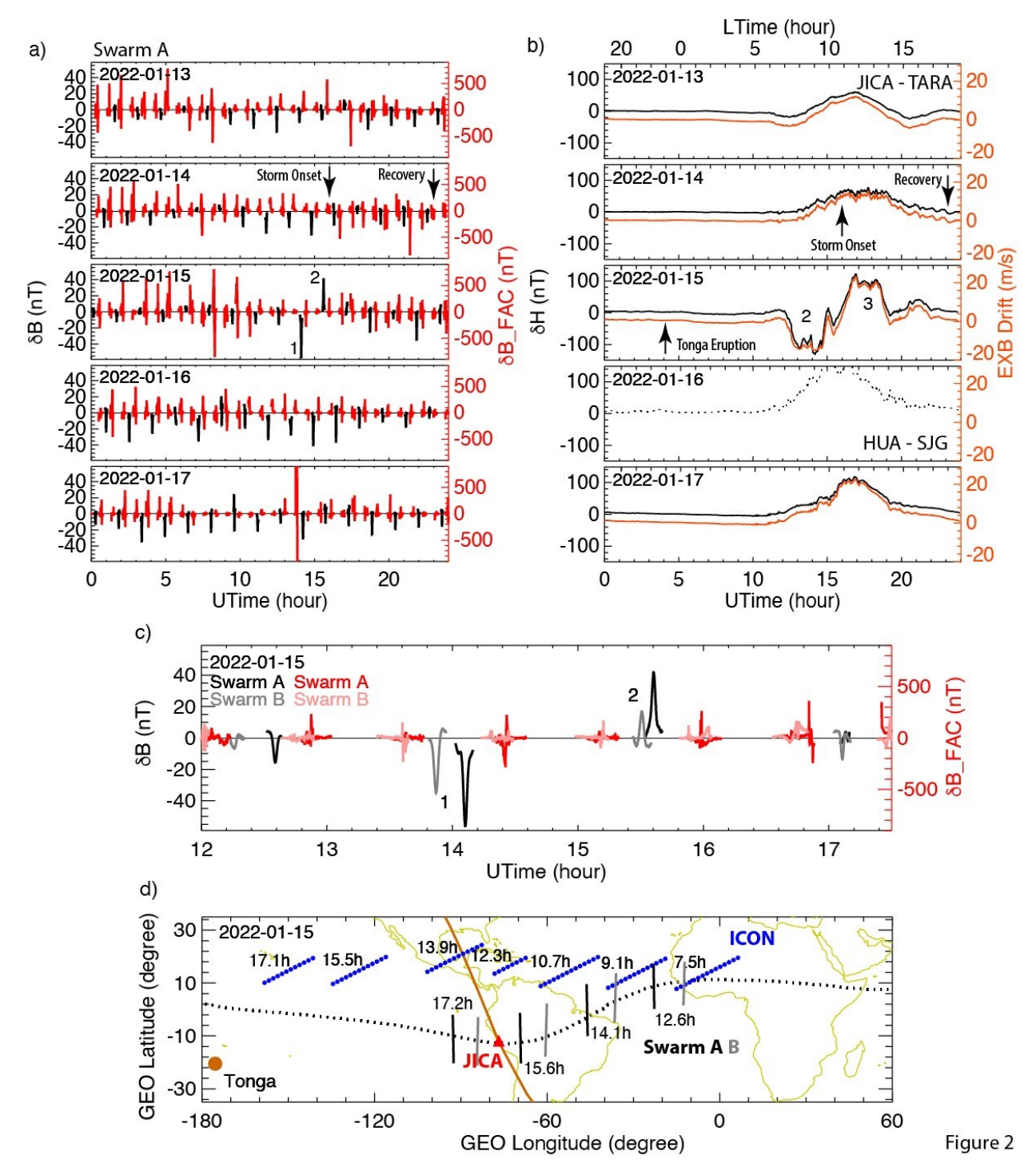


Figure 2. An overview of the observations on 13-17 January 2022. (a) The magnetic field perturbations from Swarm A. (b) The magnetic field perturbations from the ground stations near the magnetic equator and the estimated  $E \times B$  drift in the F-region. (c) Expanded view of the magnetic field perturbations from Swarm A and B on 15 January. (d) Geographic locations of the observations on 15 January.

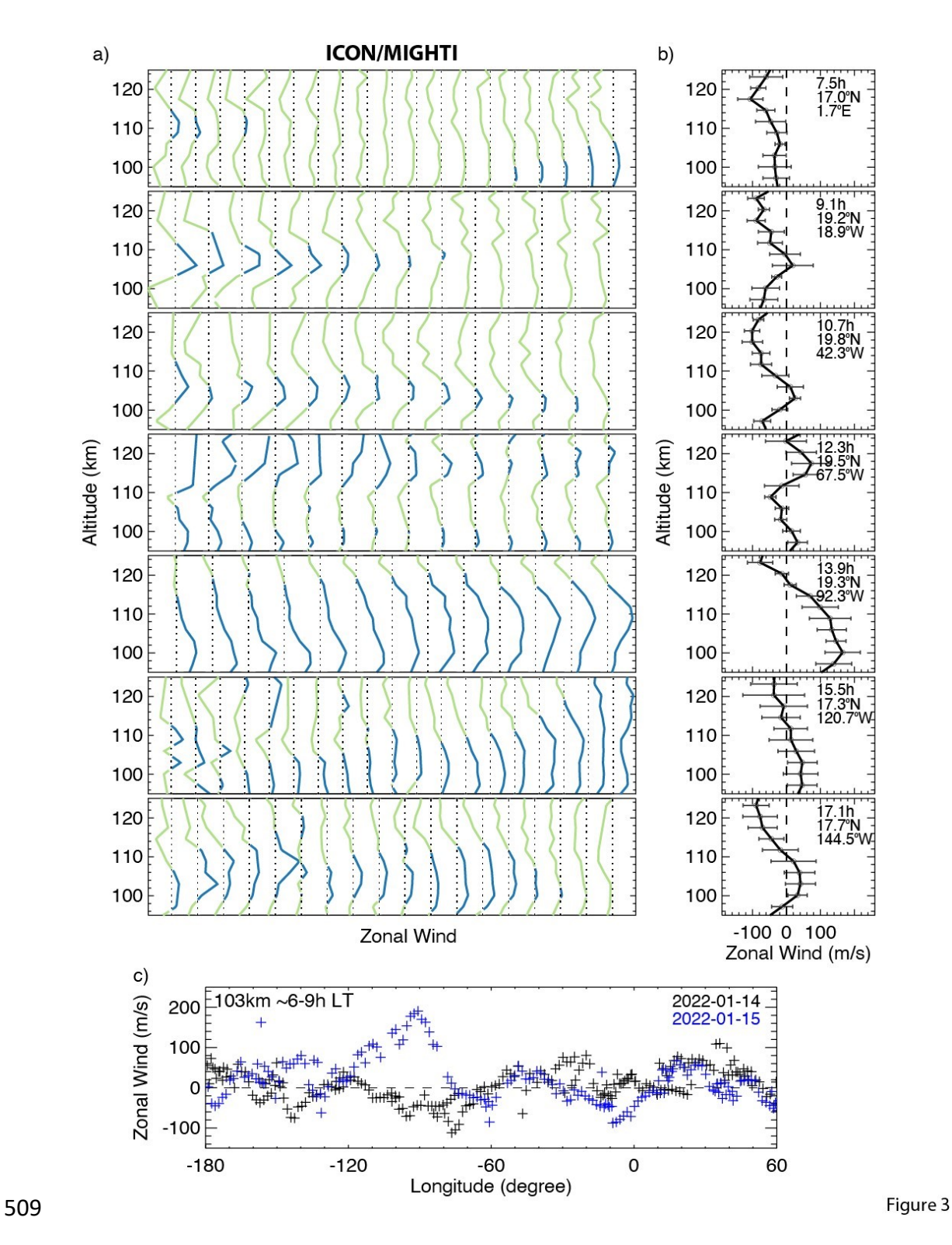


Figure 3. Daytime zonal winds observed by MIGHTI along 7 ICON orbits on 15 January 2022. (a) Altitude profiles of zonal wind sequences (blue color represents eastward winds and green color corresponds to westward winds). (b) Averaged zonal wind profiles. (c) The sequences of zonal wind observations at  $\sim$ 103 km altitude versus longitude from two days.

511512

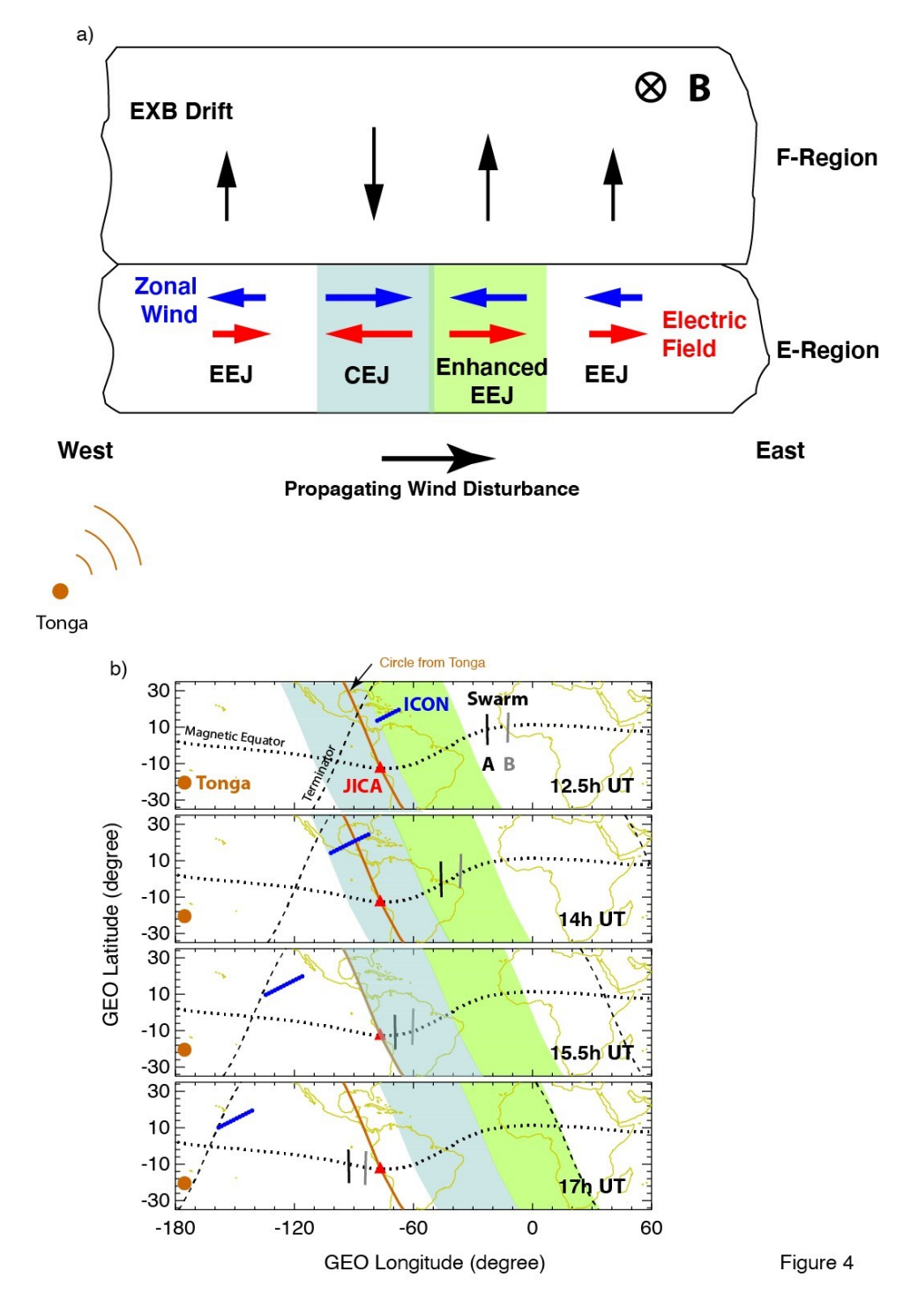


Figure 4. (a) Schematic illustration of the E- and F-region ionosphere responses to a large-scale disturbance propagating eastward from the Tonga eruption site. (b) Summary of the timelines of the observed features by the propagating disturbance.